INNER CURRENT CONTROL LOOP INFLUENCE ON ISLANDED MICROGRID DYNAMIC BEHAVIOR

Guy WANLONGO NDIWULU
UCLouvain - Belgium
guy.wanlongo@uclouvain.be

Emmanuel DE JAEGER
UCLouvain - Belgium
emmanuel.dejaeger@uclouvain.be

Angelo KUTI LUSALA
Université Kongo (UK) - DRC
kutilusala@gmail.com

ABSTRACT

A stable islanded microgrid operation is generally dictated by the adopted control strategy into the system. Droop control and master-slave control are the most used into parallel-connected inverters. However, the choice between the two is often performed in function of their complexity and that of the system configuration. It is rarely achieved in function of the microgrid dynamics. This paper proposes the system dynamics and stability as a criterion for choosing a microgrid control strategy. This is explored into the microgrid composed of photovoltaic and battery energy sources, as well as constant impedance load. The influence of inner current control loop parameters on microgrid dynamics, for both droop control and hybrid V-f and PQ control, is achieved through Small-signal stability analysis. The obtained results determine the proper control strategy from stability limits of two control methods established in the left half complex plane.

INTRODUCTION

An islanded microgrid can be considered as a low-voltage three-phase or single-phase system operating without connection to the utility grid [1]. It consists of the interconnection of distributed energy generators, energy storage devices and local loads within remote areas. It is also characterized by inverters-based energy sources, leading to relatively low system inertia. This requires using a control strategy to ensure the system integrity and stability, and to maintain the system voltage magnitude and frequency in allowable range. Most of the adopted control strategies in the literature might be classified as centralized and decentralized methods [2]. Among these techniques, droop control and master-slave control appear as the most used in parallel-interfaced inverters within islanded microgrids [2]-[5]. However, the choice between the two is often made in function of their complexity and that of the microgrid in which they are applied. For example, in [4], a discussion about control strategies is presented. The authors are focused only on their complexity for establishing the droop control advantages compared with the control approaches based on communication. Reference [2] presents a state-of-the-art of control strategies of inverter-based microgrid. Although a comparison between different control approaches is done, it is based only on the criterion of power quality and of the implemented complexity.

The choice is seldom made in function of the system dynamics and stability that might be caused by a control technique. This is generally dictated by the inner control loop, which is common to the droop control and to the hybrid grid-forming (V-f control mode) and grid-following (PQ control mode) control applied in parallel-connected converters. The impacts of this loop on the microgrid dynamics might be a better criterion, because its dynamics depends on the adopted control strategy. Small-signal stability investigation of control methods can help identify scenarios when their stability limits can occur. This will aim to specify a proper control strategy that can ensure high microgrid dynamics.

Stability issue has been investigated in the literature regarding parallel-interfaced inverters with droop control approach [5]-[6]. Although most of the papers are related to the droop coefficient impacts on microgrid dynamics and to the grid-forming inverters. Small-signal stability of microgrid with hybrid V-f and PQ control is not considered. Besides, a comparative analysis of the influence of their inner control loop on the system dynamics is not proposed.

This paper proposes a criterion for choosing the control strategy to adopt between droop control and hybrid V-f and PQ control in order to coordinate an islanded microgrid composed of photovoltaic and battery energy sources, as well as constant impedance load. The considered criterion is based on the proportional-integral (PI) inner controllers' gains on microgrid dynamics. Two small-signal dynamic models of this microgrid are derived respectively for the droop control and the hybrid control in the dq-synchronous reference frame. These models include together the grid-following control dynamics of the photovoltaic inverter and the grid-forming control dynamics of the battery inverter, without any communication between them. The position of the dominant poles compared to the stability limits in the left half plane allows to determine the performance limits of each control technique and to choose the most robust one between the two proposed approaches.

The paper is organized as follows: Section II presents the proposed topology of the islanded microgrid with control strategies. Section III gives small-signal stability models of this microgrid. This encompasses controller dynamic model, output filter and coupling inductance dynamic models, line and load models. This section also compares the dynamical performance of droop control and of hybrid control, depending on the inner current control loop parameters. Finally, section IV gives some conclusion.

ISLANDED MICROGRID ARCHITECTURE

Fig. 1 depicts the balanced three-phase islanded microgrid

composed of photovoltaic generator (PV), battery, and a constant impedance load represented by an inductance L_{load} and a resistance R_{load}. The two energy sources are connected to the system via bus 1 and bus 2, two specific inverters (photovoltaic inverter and battery inverter) and two distinct LC filters. In addition, DC-DC converter is inserted at the PV output in order to extract the maximum power (MPPT) of the PV. Constant impedance load is connected to bus 3. This one is supplied by both energy sources through two power distribution lines modeled by parameters $Z_{line1} = R_{line1} + jX_{line1}$ and $Z_{line2} = R_{line2} + jX_{line2}$.

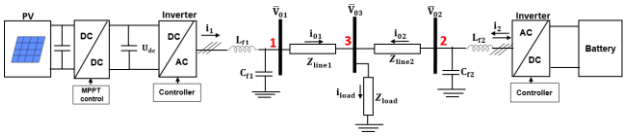

Fig. 1. Islanded microgrid architecture composed of photovoltaic and battery energy sources.

Existing droop control

Droop control can be applied to the islanded microgrid in Fig. 1 by combining two specific inverter control modes. PV inverter is controlled as a current source, while the battery one is controlled emulating the behavior of an ac voltage source. Fig. 2 and Fig. 3 present the adopted droop control structure in a dq-synchronous reference frame [7]. This hybrid control strategy aims that the PV inverter can control the injected active P_i and reactive Q_i power, and to contribute to regulate the voltage amplitude and frequency, as illustrated in Fig. 2. This one is composed of the droop control loops and of the internal current control loops implemented with PI controllers (represented by K_{Pc} and K_{Ic}). The droop loops set the current set points for the inner control loops through the droop coefficients for both voltage (m_P) and frequency (n_q).

The battery inverter regulates the system voltage V_{02d} and frequency ω based on the active P_i and reactive Q_i power at the inverter output through the reactive power droop k_{qbat} and the active power droop k_{pbat}, and $P_i^*$and Q_i^* are their reference as shown in Fig. 3. It is composed of a droop control loop followed by an inner control loop made out of a voltage loop and an internal current loop based on PI controllers. Additional virtual impedance signals are also added at the voltage control loop input in order to enhance the droop control limitations due to the output resistive impedance of the inverter [3].

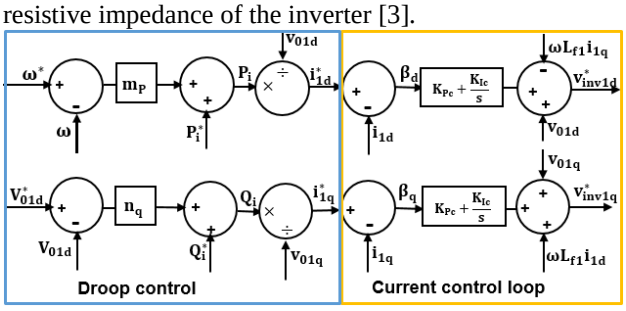

Fig. 2. Droop control algorithm implemented into the PV inverter in dq-synchronous reference frame.

The characteristic parameters in Fig. 2 and in Fig. 3 are defined bellow as

- v_{01d} and v_{02d} represent the positive sequence component of the voltage at the output of photovoltaic inverter and of battery inverter, respectively. V_{01d}^* and V_{02d}^* are their reference values. v_{01q} and v_{02q} are their quadrature components.
- ω is the frequency measurement at buses 1 and 2. ω^* its reference value.

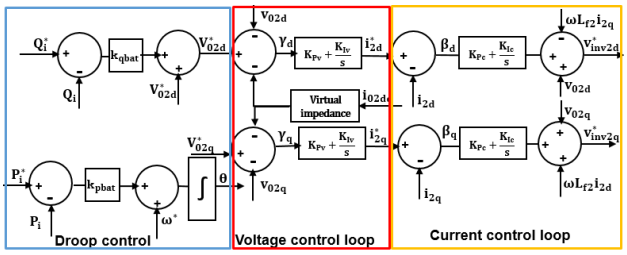

Fig. 3. Droop control algorithm implemented into the battery inverter in dq-synchronous reference frame.

Proposed hybrid V-f and PQ control

Hybrid control formulation

The proposed hybrid V-f and PQ control into islanded microgrid shown in Fig. 1 is achieved without communication. This is made possible with node role identification based on load flow concept. This developed concept consists to classifying the microgrid buses into PQ node or slack node. Therefore, the connected nodes of PV inverter (node 1) and of load (node 3) can be identified as PQ buses. In this context, PV inverter is defined as slave (PQ control) with power factor set to unity. The setting of active and reactive power can be performed through direct and quadrature components of the current (i_{1d} and i_{1q}) as established by equations (5) to (6). Quadrature component of the voltage v_{01q} is assumed to zero as explaining in [1].

$$P_i = \frac{3}{2}\left(v_{01d}i_{1d} + v_{01q}i_{1d}\right) \quad (5)$$

$$Q_i = \frac{3}{2}\left(v_{01q}i_{1d} - v_{01d}i_{1q}\right) \quad (6)$$

The battery inverter bus (node 2) is identified as a slack bus that must ensure power balancing within microgrid. It is considered as master able to impose a proper voltage magnitude and frequency (V-f control) into entire system.

PQ and V-f control structures

Control algorithms of PV inverter and of battery inverter are presented in Fig. 4 and Fig. 5, respectively. They are based on the PI controllers. The proposed PQ control structure in Fig. 4 is composed of two-loops control composed of DC voltage control loop and of current control loop. The external loop controls DC voltage U_{dc} at the PV inverter input in order to enable the injection of maximum power produced by MPPT controller to the AC system. This loop also provides the set point to the direct component of the current i_{1d}. Whereas, reference value of quadrature component of the current i_{1q}^* is set to zero, because the power factor is chosen to be equal to 1.

Fig. 5 illustrates the V-f control structure. It is composed

of two-loops, an external voltage loop and an internal current control loop. The external loop controls the system voltage amplitude via control of the direct and quadrature components of the voltage v_{o2dq}. It also sets the reference values to the current control loop (i_{2dq}). Note that feedforward terms Fi_{o2dq} and $v_{o1(2)dq}$, and decoupling terms $\omega C_{f2} v_{o2dq}$ and $\omega L_{f1(2)} i_{1(2)dq}$ are added at the output of the two control loops.

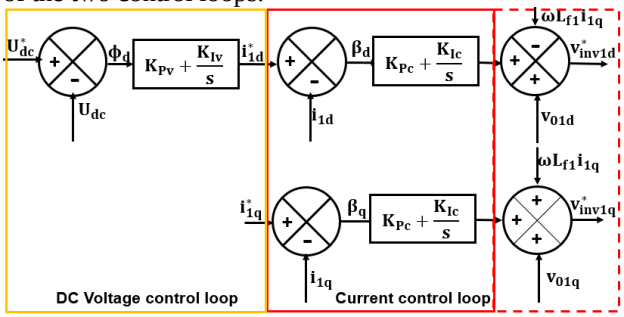

Fig. 4. PQ control structure implemented into the PV inverter in dq-synchronous reference frame.

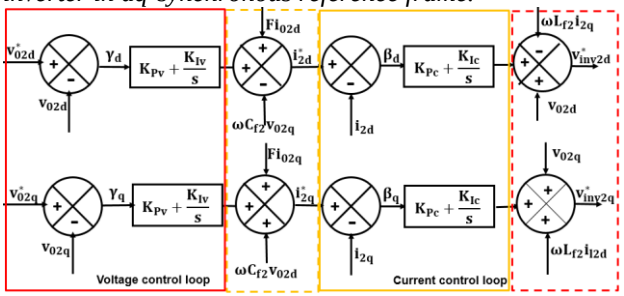

Fig. 5. V-f control structure implemented into the battery inverter in dq-synchronous reference frame.

STABILITY ANALYSIS RESULTS

Small-signal modeling of the droop control

Fig. 6 gives the state-space model of the proposed islanded microgrid. It is composed of PV inverter model, network and load model, and of battery inverter model. Sub-models of controllers, LC filter and of coupling impedance form each inverter dynamic model. Controller model of each inverter consists of power control model and of inner control model. Most of the used mathematical formulation of the power control model is based on [6]. Inner control loops models depend on the grid-forming inverter and of grid-following inverter.

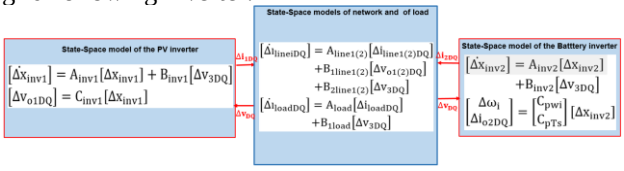

Fig. 6. Small-signal model of islanded microgrid based on droop control approach.

PV inverter small-signal model

Equations (8) to (11) give the state vector $[\Delta x_{inv1}]$, dynamic matrix A_{inv1}, input matrix B_{inv1} and output matrix C_{inv1} of the PV inverter dynamic model, as illustrated in Fig. 6. Where

- δ is the phase angle. P_i and Q_i are the output active and reactive power of the PV inverter.
- β_{dq} are the direct and quadrature components of output signal of the current comparator.
- i_{1dq} are the components of the current on LC filter inductance. v_{01dq} are the voltage components at the LC filter output.
- i_{01dq} are the current components at the LC filter output.
- T_s is the transformation matrix which allows to translate the state-space model of the network, load and of the inverter to the common reference frame of one of the individual inverters [6].
- $v_{o1(2)DQ}$ and v_{3DQ} are the obtained components of the voltage to the buses 1 to 3, in D- and Q-axis common reference frame [6].

$$[\Delta x_{inv1}] = [\Delta\delta \ \Delta P_i \ \Delta Q_i \ \Delta\beta_{dq} \ \Delta i_{1dq} \ \Delta v_{01dq} \ \Delta i_{01dq}]^T \quad (8)$$

$$A_{inv1} = \begin{bmatrix} A_p & 0 & B_p \\ F_{c1}C_1C_{p\omega} & 0 & F_{c1}C_2 + F_{c2} \\ B_{LCL}G_{c1}C_1C_{p\omega} & B_{LCL}C_c & A_{LCL} + B_{LCL}(G_{c1}C_2 + G_{c2}) \end{bmatrix}_{11x11} \quad (9)$$

$$B_{inv1} = [0 \quad 0 \quad B_{LCl2}T_s^{-1}]^T_{11x2} \ (10) \text{ and } C_{inv1} = [0 \quad T_s]_{2x11} \quad (11)$$

Submatrices of equations (9) to (11) are determined by

$$A_p = \begin{bmatrix} 0 & -1/m_p & 0 \\ 0 & -\omega_c & 0 \\ 0 & 0 & -\omega_c \end{bmatrix}; C_{p\omega} = \begin{bmatrix} 0 & 0 & -1/n_q \\ 0 & -1/m_p & 0 \end{bmatrix}; C_2 = \begin{bmatrix} 0 & 0 & 0 & 0 & 0 & 1 \\ 0 & 0 & -m_p/V_d & 0 & 1 & 0 \end{bmatrix}$$

$$C_1 = \begin{bmatrix} n_q/V_d & 0 \\ 0 & m_p/V_d \end{bmatrix}; B_p = \begin{bmatrix} 0 & 0 & 0 & 0 & 0 & 0 \\ 0 & 0 & \omega_c I_{od} & \omega_c I_{oq} & \omega_c V_{od} & \omega_c V_{oq} \\ 0 & 0 & \omega_c I_{oq} & -\omega_c I_{od} & -\omega_c V_{oq} & \omega_c V_{od} \end{bmatrix}; G_{c1} = \begin{bmatrix} K_{Pc} & 0 \\ 0 & K_{Pc} \end{bmatrix}$$

$$F_{c2} = \begin{bmatrix} -1 & 0 & 0 & 0 & 0 & 0 \\ 0 & -1 & 0 & 0 & 0 & 0 \end{bmatrix}; F_{c1} = \begin{bmatrix} 1 & 0 \\ 0 & 1 \end{bmatrix}; G_{c2} = \begin{bmatrix} -K_{Pc} & -\omega L_f & 1 & 0 & 0 & 0 \\ \omega L_f & -K_{Pc} & 0 & 1 & 0 & 0 \end{bmatrix}$$

$$B_{LCL} = \begin{bmatrix} 0 & 1/L_f & 0 & 0 & 0 & 0 \\ 1/L_f & 0 & 0 & 0 & 0 & 0 \end{bmatrix}^T; B_{LCL2} = \begin{bmatrix} 0 & 0 & 0 & 0 & 0 & -R_C/L_C \\ 0 & 0 & 0 & 0 & -R_C/L_C & 0 \end{bmatrix}^T$$

$$A_{LCL} = \begin{bmatrix} -R_f/L_f & \omega & -1/L_f & 0 & 0 & 0 \\ -\omega & -R_f/L_f & 0 & -1/L_f & 0 & 0 \\ 1/C_f & 0 & 0 & \omega & -1/C_f & 0 \\ 0 & 1/C_f & -\omega & 0 & 0 & -1/C_f \\ 0 & 0 & 1/L_C & 0 & -R_C/L_C & \omega \\ 0 & 0 & 0 & 1/L_C & -\omega & -R_C/L_C \end{bmatrix}; C_C = \begin{bmatrix} K_{Ic} & 0 \\ 0 & K_{Ic} \end{bmatrix}$$

Battery inverter small-signal model

The developed global model is also referring to Fig. 6. Equation (12) defines the state vector. Where

- i_{02dq} are the current components at the LC filter output of battery inverter. v_{02dq} are the voltage components at the LC filter output.
- γ_{dq} are the direct and quadrature components of output signal of the voltage comparator.
- i_{2dq} are the components of the current on LC filter inductance.

Dynamic matrix A_{inv2}, output matrix C_{inv2} and input matrix B_{inv2} are given by equations (13) to (15).

$$[\Delta x_{inv2}] = [\Delta\delta \ \Delta P_i \ \Delta Q_i \ \Delta\gamma_{dq} \ \Delta\beta_{dq} \ \Delta i_{2dq} \ \Delta v_{02dq} \ \Delta i_{02dq}]^T \quad (12)$$

$$A_{inv2} = \begin{bmatrix} A_p & 0 & 0 & B_p \\ G_1C_{pv} & 0 & 0 & G_2 \\ F_{c1}A_1C_{pv} & F_{c1}C_v & 0 & F_{c1}A_2 + F_{c2} \\ B_{LCL}F_{c1}A_1C_{pv} & B_{LCL}F_{c1}C_v & B_{LCL}C_C & A_{LCL} + B_{LCL}(F_{c1}A_2 + F_{c2}) \end{bmatrix}_{13x13} \quad (13)$$

$$B_{inv2} = \begin{bmatrix} 0_{6x1} & -\sin\delta_o/L_C & -\cos\delta_o/L_C \\ 0_{6x1} & -\cos\delta_o/L_C & \sin\delta_o/L_C \end{bmatrix}^T_{13x2} \quad (14)$$

$$C_{inv2} = \begin{bmatrix} C_{p\omega i} \\ C_{pTs} \end{bmatrix} = \begin{bmatrix} 0 & -mp & 0_{1x9} & 0 & 0 \\ 0 & 0 & 0_{1x9} & \cos\delta_o & -\sin\delta_o \\ 0 & 0 & 0_{1x9} & \sin\delta_o & \cos\delta \end{bmatrix}_{3x13} \quad (15)$$

Submatrices of the dynamic matrix are defined by

$$G_1 = \begin{bmatrix} 1 & 0 \\ 0 & 1 \end{bmatrix}; G_2 = \begin{bmatrix} 0 & 0 & -1 & 0 & -R_v & 0 \\ 0 & 0 & 0 & -1 & 0 & -R_v \end{bmatrix}; C_v = \begin{bmatrix} K_{Iv} & 0 \\ 0 & K_{Iv} \end{bmatrix}$$

$$A_1 = \begin{bmatrix} K_{Pv} & 0 \\ 0 & K_{Pv} \end{bmatrix}; A_2 = \begin{bmatrix} 0 & 0 & -K_{Pv} & 0 & -R_v & 0 \\ 0 & 0 & 0 & -K_{Pv} & 0 & -R_v \end{bmatrix}$$

Dynamical models of the line and of the load

Small-signal models of lines and of constant impedance load are given in Fig. 6. Its matrices are equivalent than that proposed in [8]. i_{load} and i_{line} are the currents on the power distribution lines and the load impedance.

Small-signal modelling of the hybrid control

Fig. 7 depicts the small-signal model in which state-space model of lines and of load are the same than in Fig. 6.

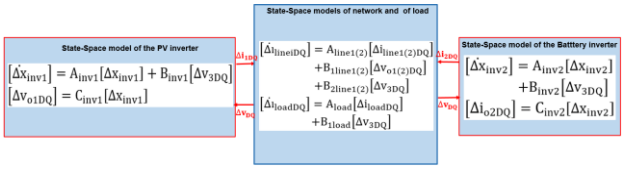

Fig. 7. Small-signal model of islanded microgrid based on hybrid V-f and PQ control approach.

PV inverter state-space model

Equations (16) and (17) give the state-space vector and the dynamic matrix of the PV inverter model in which ϕ_{dq} represents the components of output signal of the DC voltage comparator (Fig. 4).

$$[\Delta x_{inv1}] = [\Delta\phi_{dq} \quad \Delta\beta_{dq} \quad \Delta U_{dc} \quad \Delta i_{ldq} \quad \Delta v_{0dq} \quad \Delta i_{0dq}]^T \quad (16)$$

$$A_{inv1} = \begin{bmatrix} 0 & 0 & B_{v2} \\ F_{C1}C_V & 0 & F_{C1}D_{v2} + B_{C2} \\ B_{LC1}G_{C1}C_V & B_{LC1}C_C & A_{LC} + B_{LC1}(G_{C1}D_{v2} + D_{C2}) \end{bmatrix}_{11x11} \quad (17)$$

The submatrices related to equation (17) are given by

$$B_{v2} = \begin{bmatrix} -1 & 0_{1x6} \\ 0 & 0_{1x6} \end{bmatrix}; D_{v2} = \begin{bmatrix} -K_{Pv} & 0_{1x6} \\ 0 & 0_{1x6} \end{bmatrix}; B_{c2} = \begin{bmatrix} 0 & -1 & 0 & 0_{1x4} \\ 0 & 0 & -1 & 0_{1x4} \end{bmatrix}$$

$$D_{c2} = \begin{bmatrix} 0 & -K_{Pc} & -\omega L_f & 1 & 0 & 0 & 0 \\ 0 & \omega L_f & -K_{Pc} & 0 & 1 & 0 & 0 \end{bmatrix}; A_{LC} = [0 \quad A_{LCL}]; B_{LC1} = \begin{bmatrix} 0 \\ B_{LCL} \end{bmatrix}$$

Battery inverter state-space model

Equations (18) and (19) characterize this model.

$$[\Delta x_{inv2}] = [\Delta\gamma_{dq} \; \Delta\beta_{dq} \; \Delta i_{ldq} \; \Delta v_{0dq} \; \Delta i_{0dq}]^T \quad (18)$$

$$A_{inv2} = \begin{bmatrix} 0 & 0 & A_{v2} \\ F_{C1}C_v & 0 & F_{C1}E_{v2} + F_{C2} \\ B_{LCL}G_{C1}C_v & B_{LCL}C_C & A_{LCL} + B_{LCL}(G_{C1}E_{v2} + G_{C2}) \end{bmatrix}_{10x10} \quad (19)$$

$$B_{inv2} = [0 \; 0 \; B_{LCL2}T_s^{-1}]_{10x2}^T; \quad C_{inv2} = [0 \; 0 \; 0 \quad 0 \; T_s]_{2x10}$$

The submatrices of this dynamic model are determined by

$$A_{v2} = \begin{bmatrix} 0 & 0 & -1 & 0 & 0 & 0 \\ 0 & 0 & 0 & -1 & 0 & 0 \end{bmatrix}; E_{v2} = \begin{bmatrix} 0 & 0 & -K_{Pv} & 0 & F & 0 \\ 0 & 0 & 0 & -K_{Pv} & 0 & F \end{bmatrix}$$

Modelling results

Table I summarizes the main considered microgrid factors and the related parameters to small-signal dynamic models [6],[8]. Noted that the same characteristics of LC filters and of lines, and constant droop coefficients are used.

The poles of the two developed dynamic models of the islanded microgrid in function of the two adopted control strategies are individually computed. Then, their sensitivity is examined through graphical mapping. The locations of the dominant poles are identified in the complex plane by considering the variation of internal current control loop gains. The loci of dominant poles related to the two derived models are explored in order to establish stability limits of each model.

Table I Main Parameters of the system components

Coupling impedance	Inductance (L_C) :0,5mH Resistance (R_C): 0,05Ω
LC Filter	Inductance (L_f): 5mH ; Capacitance (C_f): 200µF $f_{sw} = 500Hz$; Resistor :$R_f = 0,5\Omega$
RL load	400V ; 30kW ; 0,25kVar ; $V_{0d} = v_{0d}^* = 320V$; $V_{0q} = v_{0q}^* = 0$
Controllers	Droop coefficients: $k_{pbat} = 9{,}4e^{-5}$; $k_{qbat} = 1{,}3e^{-3}$ $m_p = k_{pbat}$; $n_q = k_{qbat}$; $R_v = 0,2\Omega$ Inner loops : $\omega_{nIn} = 4000rad/s$; $K_{Ic} = 53e3$; $K_{Pc} = 25,03$ Outer loops: $\omega_{nEx} = 400rad/s$; $K_{Iv} = 390$; $K_{Pv} = 0,14$ Damping factor $\zeta = 0,84$; fn = 50Hz
Sources	Photovoltaic inverter : 30kW and Battery inverter : 30kVA
Others	F=0,98 ; $\delta_o = 1{,}9e^{-3}$; $I_{0d} = 11,4$ A ; $I_{0d} = 1,25$A

Dominant poles given steady-state conditions

Droop control method: Fig. 8. presents the poles plotted in the complex plane for given steady-state conditions. The corresponding modes are numbered from 1 to 5. Modes 1 are related to power controller by real and reactive power, and phase angle. Second, modes 2 and modes 4 are linked to the internal current control loops. The obtained results show that oscillation frequencies of these poles are very close, while their damping factors are distinct for modes 2. The trajectory of these poles in the left half plane can be considered as a specific criterion to identify an adequate control strategy between two developed control methods. Then, modes 3 are due to the LC filter capacitance. Finally, modes 5 are associated to the coupling impedance and their localization is linked to the considered values of inductor and resistor. One negative real pole of the mode 5 is found as dominant pole in steady-state conditions.

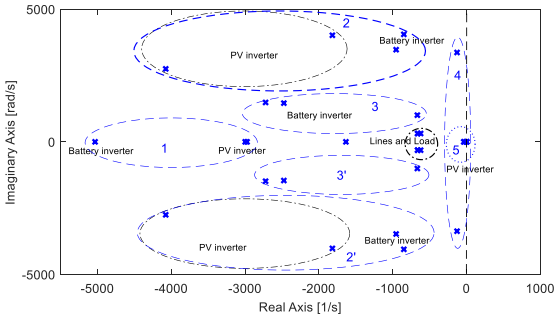

Fig. 8. Small-signal analysis results for the droop control

Hybrid V-f and PQ control method: Fig. 9 shows the poles plotted in the complex plane. They are grouped in three groups numbered from 1 to 3. The related poles of group 1 are associated to the internal current control loop. Whereas groups 2 to 3 are linked to the LC filter parameters and to the external voltage control loops. One conjugate pair of the complex poles 3 appear to be the dominant poles. The trajectory of poles 1 in the left half plane dictates the system dynamics and stability. Compared to the presented previous results in Fig. 8, damping factors of poles 1 between the two inverters are close to each other.

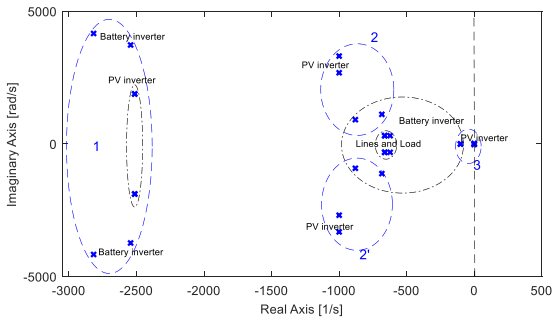

Fig. 9. Small-signal analysis results for the hybrid V-f and PQ control approach.

Comparison of the two small-signal models

The comparison is made by considering the impacts of the value of the proportional gain Kpc of the current control loops, both for the droop control and hybrid control strategies. Fig. 10 and Fig. 11 show the results obtained by changing the value of the proportional gain. They show that the dominant modes 5 (Fig. 8) and modes 3 (Fig. 9) are less affected than the modes 2 and modes 4 (Fig. 10), and the modes 1 (Fig. 11), when decreasing the current controllers gain. Under these conditions, the system stability in Fig. 10 is mostly related to modes 2 and 4, while by the mode 1 in Fig. 11. Fig. 10 shows that all the poles are affected. It also shows that with the same proportional gain value, the stability limits are not the same for both parallel inverters. Poles 4 of the PV inverter become unstable before poles 2 of the battery inverter and of the PV inverter. However, the situation can be improved with the hybrid control as illustrated in Fig. 11.

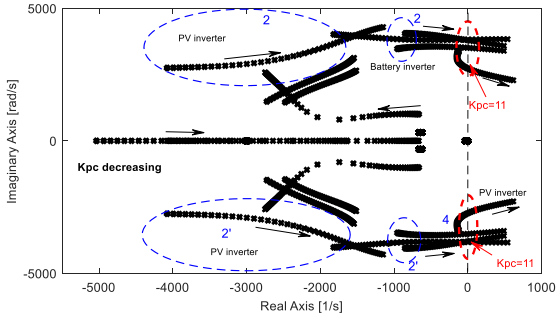

Fig. 10. Impacts of proportional gain Kpc of the current control loops on the stability limits of the poles. Case of the small-signal model of islanded microgrid implemented with droop control: $0{,}10 \leq Kpc \leq 25{,}03$

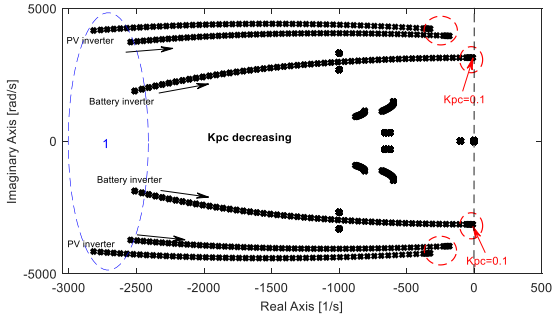

Fig. 11. Impacts of proportional gain Kpc of the current control loops on the stability limits of the poles. Case of the small-signal model of islanded microgrid implemented with hybrid V-f and PQ control: $0{,}10 \leq Kpc \leq 25{,}03$

CONCLUSION

System dynamics and stability have been explored in order to determine a proper control strategy able to coordinate an islanded microgrid composed of photovoltaic and battery energy sources, as well as constant impedance load. Droop control and hybrid V-f and PQ control have been introduced and compared from in-depth small-signal stability analysis. The developed state-space models of the microgrid related to each control method have been examined from the locations of dominant poles in the left half complex plane. The trajectory of these poles associated to the variation of inner current control loop gains have allowed to establish the stability limits of the two control approaches. The obtained results have shown that the hybrid control applied without communication provides better dynamical performance than droop control method.

REFERENCES

[1] G. Wanlongo Ndiwulu, E. De Jaeger, A. Kuti Lusala, 2017, "Inner Control Loops Approach to Control the Islanded Photovoltaic Microgrid", *Proceedings IEEE AFRICON conference, Cape Town*, 1204-1209.

[2] M. H. Andishgar, E. Gholipour, R.-A. Hooshmand, 2017, "An overview of control approaches of inverter based microgrids in islanding mode of operation", *Renewable and Sustainable Energy Reviews* 80, 1043–1060.

[3] T.L. Vandoorn, J.D.M. DeKooning, B. Meersman, L. Vandevelde, 2013, "Review of primary control strategies for islanded microgrids with power-electronic interfaces", *Renewable and Sustainable Energy Reviews* 19, 613–628.

[4] U.B. Tayab, M.A.B. Roslan, L.J. Hwai, M. Kashif, 2017, "A review of droop control techniques for microgrid", *Renewable and Sustainable Energy Reviews* 76, 717–727.

[5] Y. Li, L. Fan, 2017, "Stability Analysis of Two Parallel Converters With Voltage–Current Droop Control", *IEEE Transactions on Power Delivery*, Vol.32, No.6, 2389-2397.

[6] N. Pogak, M. Prodanovic, T. C. Green, 2007, "Modeling, Analysis and Testing of Autonomous Operation of an Inverter-Based Microgrid", *IEEE Transactions on Power Electronics*, vol.22, 613-625.

[7] J. Rocabert, A. Luna, F. Blaabjerg, P. Rodriguez, 2012, "Control of Power Converters in AC Microgrids", *IEEE Transactions on Power Electronics*, Vol. 27, No. 11,4734-4749.

[8] G. Wanlongo Ndiwulu, E. De Jaeger, A. Kuti Lusala, 2018, "Local stability performance analysis of islanded microgrid based on inner control loops approach", *CIRED Workshop 2018*.